Journal of Zhejiang University-SCIENCE A (Applied Physics & Engineering)
ISSN 1673-565X (Print); ISSN 1862-1775 (Online)
www.jzus.zju.edu.cn; www.springerlink.com
E-mail: jzus@zju.edu.cn

Numerical study on the morphology of a liquid-liquid pintle injector element primary breakup spray*

Rui ZHOU, Chi-bing SHEN†‡, Xuan JIN

Science and Technology on Scramjet Laboratory, College of Aerospace Science and Engineering, National University of Defense Technology, Changsha 410073, China

†E-mail: cbshen@nudt.edu.cn

Received Dec. 11, 2019; Revision accepted Mar. 20, 2020; Crosschecked Aug. 4, 2020

Abstract: Primary breakup in a liquid-liquid pintle injector element at different radial jet velocities is investigated to elucidate the impingement morphology, the formation of primary breakup spray half cone angle, the pressure distribution, the liquid diameter distribution, and the liquid velocity distribution. With a sufficient mesh resolution, the liquid morphology can be captured in a physically sound way. A mushroom tip is triggered by a larger radial jet velocity and breakup happens at the tip edge first. Different kinds of ligament breakup patterns due to aerodynamic force and surface tension are captured on the axial sheet. A high pressure core is spotted at the impinging point region. A larger radial jet velocity can feed more disturbances into the impinging point and the axial sheet, generate stronger vortices to promote the breakup process at a longer distance, and form a larger spray half cone angle. Because of the re-collision phenomenon the axial sheet diameter does not decrease monotonically. The inner rim on the axial sheet shows a larger diameter magnitude and a lower velocity magnitude due to surface tension. This paper is expected to provide a reference for the optimum design of a liquid-liquid pintle injector.

Key words: Pintle injector element; Liquid-liquid impingement; Primary breakup; Volume of fluid-to-discrete phase model (VOF-to-DPM) simulation; Adaptive mesh refinement (AMR) method

https://doi.org/10.1631/jzus.A1900624 **CLC number:** V23; V43

1 Introduction

The pintle injector is used mainly in liquid rocket engine applications as a propellant injection system like shear or swirl coaxial injectors because of its combustion stability, high throttling capability, and simple structure (Fang and Shen, 2017). The pintle injector concept was developed by the TRW Corporation (the USA), and was successfully used in the lunar module descent engine in 1969 (Elverum and Miller, 1967; Dressler, 2006; Giuliano and Adamski, 2007).

The pintle injector is a typical cross flow type liquid-liquid, liquid-gas or gas-gas injector (Nardi and Pimenta, 2015). There is an annular gap through which one liquid flows through the surface of the pintle's main body to its top and forms a liquid annular sheet of specified thickness in the axial direction. Near the pintle top, there are several discrete orifices along the circumference or a continuous gap where the radial liquid jets are injected and impinge with the axial liquid, forming a liquid spray.

The characteristics of a pintle injector are relevant to many factors such as the skip distance, BF, TMR, LMR, and the spray half cone angle. The skip distance refers to the distance from the axial liquid sheet entrance point to the point of contact with the radial orifice jet. BF is known as the block factor. TMR is defined as the ratio of the total momentum rate of the radial jet to that of the axial sheet. LMR,

‡ Corresponding author

* Project supported by the National Natural Science Foundation of China (No. 11572346)

ORCID: Rui ZHOU, https://orcid.org/0000-0003-4620-9996

where "L" means local, refers simply to the area of a single radial orifice, and for the axial propellant, refers only to the area of propellant expected to collide with an individual radial jet. In this paper, there is only one radial hole and the normal pintle axial concentric circular slot is simplified to a rectangular slot, so LMR is accurate in illustrating the ratio of the momentum of one radial hole to that of the axial sheet colliding with this one radial hole. The spray half cone angle, α, is the angle between the resultant velocity direction and the axial velocity direction. More details of the pintle injector are described in (Dressler, 2000).

Public numerical research on pintle injectors is limited although some experiments have been reported. Son and Jaye (2015) investigated the effects of TMR and Weber number (*We*) on the spray characteristics of the pintle injector for liquid-gas propellants under multiple injection conditions and concluded that the spray half cone angle had an exponentially decreasing correlation with TMR divided by *We*. Ninish and Nandakumar (2018) investigated the spray pattern of the liquid-liquid pintle injector under different TMR conditions, concluding that it is radial liquid jets that generate wave instabilities on the axial liquid sheet surface, and a higher velocity of the radial liquid jets leads to better atomization compared with a lower velocity. Cheng et al. (2017, 2019) investigated the spray half cone angle of a liquid-liquid pintle injector under different operating conditions and developed a prediction equation of the spray half cone angle: $\cos\alpha=1/(1+\mathrm{TMR})$. This prediction equation agreed well with experimental results. James and Jacob (2019) raised a new aspect of LMR by investigating the relationships among spray half cone angle, LMR, and the geometry of radial orifices in a liquid-liquid pintle injector. Results showed that at a certain LMR, the spray half cone angle is largely independent of the geometry of the pintle radial orifices. Similarly, Kazuki and Shinji (2015, 2017) experimented with a planar pintle injector to investigate the relationships of combustion efficiency with mass flow ratio of oxidizer to fuel, focusing, for better visualization, on the characteristics of one axial liquid impinging with one radial liquid.

Apart from the experimental studies mentioned above which focus on the spray half cone angle of the pintle injector, there have been other studies mainly revealing the droplet distribution. Ninish and Nandakumar (2018) investigated the influence of TMR on droplet formation and size distribution of the liquid-liquid pintle injector, concluding that a lower axial liquid velocity increases the liquid sheet thickness and contributes to a larger droplet size. Kanmaniraja and Keonwoong (2018) investigated the effect of mass flow rate and axial gap width on the droplet distribution characteristics of a liquid-gas pintle injector, concluding that by increasing the mass flow rate of liquid at the lower axial gap width there results in a narrower spray half cone angle, causing poorer mixing. The wider the spray half cone angle is, the wider is the range of a mass fraction of droplet distribution forming along the radial position.

All in all, there have been several studies on the spray characteristics of the pintle injector, but the focus of these studies has been rather limited, and the morphology of the impingement is not mentioned although quantitative analysis has been summarized. The spray half cone angle has been well discussed and some scholars have given a prediction formula based on the relationship between spray half cone angle and TMR, indicating that the higher the radial momentum is, the larger the half spray cone angle is. Furthermore, that a BF around 0.5 gives the best spray pattern is a generally known empirical criterion. These studies need to be further discussed and there are other aspects like spray distribution morphology that remain unclear. More importantly, the impingement is really a transient moment which lasts for only about one millisecond or less, and it is difficult to capture its specific details and the streamline cannot be obtained through experiments. Therefore, more systematic numerical research is needed.

In this paper, a liquid-liquid pintle injector element is used for better visualization in order to put emphasis specifically on how one radial orifice jet with different velocities impinges with the axial rectangular sheet. The impingement morphology, the formation of spray half cone angle, the pressure distribution, the liquid diameter distribution, and the liquid velocity distribution are discussed.

2 Simulation apparatus

2.1 Target flow domain

The test instrument is shown in Fig. 1a (Cheng et al., 2019). The experimental study will be described

later. Based on the structure of the test instrument, the skip distance is 10 mm (L_s=10 mm), and the numerical simulation domain is a cuboid in Cartesian equidistant grid system with length of 60 mm (L=60 mm), width of 15 mm (W=15 mm), and height of 25 mm (H=25 mm) as depicted in Fig. 1b. Four perspectives marked view a, view b, view c, and view d are used to describe the results comprehensively. Surfaces in red, green, and blue are set as velocity inlet, pressure outlet, and wall. Both the axial sheet and the radial jet are simulated as water and the physical characteristics are shown in Table 1. The axial sheet is injected along the x+ direction through a rectangular slot. The radial jet is injected along the y+ direction with different velocities through an orifice. The axial sheet and the radial jet will impact vertically at point A (i.e. the impinging point) shown in Fig. 1b, where the formation of the spray half cone angle starts to develop. The Z direction is the spanwise direction. The calculation formulas for We and Reynolds number Re are $We=\rho v^2 l/\sigma$ and $Re=\rho v l/\mu$, where ρ is the fluid density, v is the fluid velocity, σ is the surface tension coefficient, μ is the viscosity, and l is the characteristic length. For the axial sheet, the characteristic length is calculated by l=length×thickness/[2×(length+thickness)], and for the radial jet, the characteristic length is equal to its diameter. Detailed flow conditions are shown in Table 2.

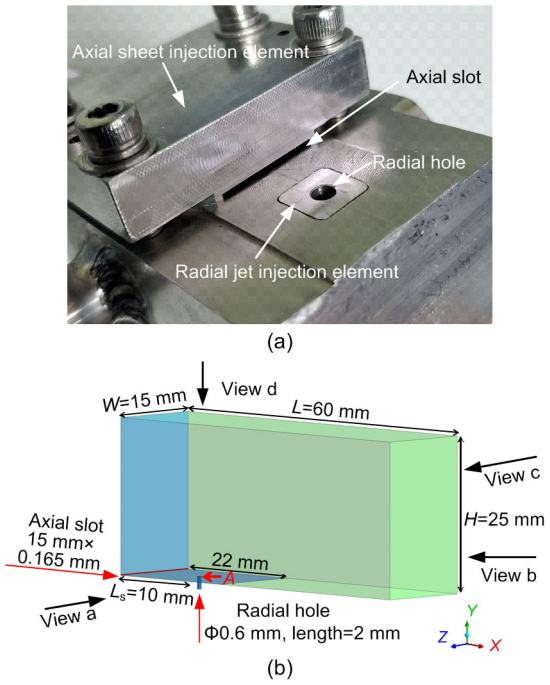

Fig. 1 Simulation domain setup: (a) test instrument; (b) simulation domain

References to color refer to the online version of this figure

2.2 Numerical methods

For the numerical simulation we used the volume of fluid-to-discrete phase model (VOF-to-DPM) model in commercial software ANSYS 19.2, considering only the primary breakup. The turbulence model is a shear-stress transport k-w model, including a curvature correction. The initial liquid volume is predicted by the VOF model, while the particles detached from the liquid volume are simulated by DPM. In the VOF approach, the volume fraction of the liquid is stored in each mesh. The gas-liquid interface is tracked by explicit discretization schemes. The VOF-to-DPM model transition algorithm automatically tracks liquid masses that have detached from the liquid core of the VOF solution. It then assesses their feasibility for the VOF-to-DPM conversion requirements. If the liquid satisfies the user-specified requirements, such as lump size and asphericity, it is removed from the resolved liquid in the VOF simulation and converted to a particle parcel in a Lagrangian formulation. Selected pressure implicit split

Table 1 Simulation material physical characteristics

Direction	Medium	Temperature (K)	Viscosity (kg/(m·s))	Surface tension (N/m)
Axial Radial	Water	300	0.001	0.07

Table 2 Flow conditions of liquids

Case	Axial liquid (rectangular sheet)					Radial liquid (orifice jet)					TMR	LMR
	Length (mm)	Thickness (mm)	V_a (m/s)	We	Re	Diameter (mm)	Pressure drop (MPa)	V_r (m/s)	We	Re		
B	15	0.165	49.1	11253	15982	0.6	0.7	30.0	7699	17928	0.04	0.32
B-1	15	0.165	49.1	11253	15982	0.6	1.1	37.5	12066	22445	0.07	0.51
B-2	15	0.165	49.1	11253	15982	0.6	1.5	43.8	16459	26213	0.09	0.70

V_a is the liquid impinging velocity in axial (x+) direction; V_r is the liquid impinging velocity in radial (y+) direction

operator (PISO) for the pressure-velocity coupling scheme and geo-reconstruct for the spatial discretization, increase the pressure and momentum under-relaxation factors to values close to 1.

The main mechanism is illustrated in Fig. 2. The present work set the time step size as 5×10^{-8} s and the maximum iterations per time step as 25. The mesh quantity was controlled to be less than 750000 at the end of the numerical simulation.

The governing equations to be solved are 3D Navier-Stokes equations, i.e.

$$\begin{cases}\nabla\cdot v=0,\\ \dfrac{\partial\rho v}{\partial t}+\nabla\cdot(\rho v^2)=-\nabla p+\mu\Delta v+F,\end{cases} \tag{1}$$

where t is the time, p is the pressure, and F is the surface tension term. Both liquid and gas are considered as Newtonian fluids.

To simplify the equation, the effect of disturbances from the upstream inlets in both axial and radial directions is ignored.

In the VOF simulation, C, the function of fluid volume ratio is defined as the ratio of fluid volume to mesh element volume, which can be written as

$$C=\begin{cases}0, & \text{gas},\\ (0,1), & \text{gas+liquid},\\ 1, & \text{liquid}.\end{cases} \tag{2}$$

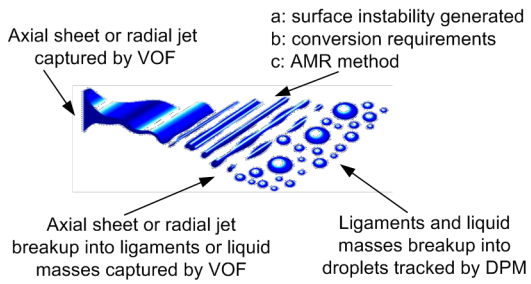

Fig. 2 Illustration of the main numerical simulation mechanism

The physical properties in the control element are calculated by C. The density and viscosity are interpolated as

$$\begin{aligned}\rho&=C\rho_{\mathrm{l}}+(1-C)\rho_{\mathrm{g}},\\ \mu&=C\mu_{\mathrm{l}}+(1-C)\mu_{\mathrm{g}},\end{aligned} \tag{3}$$

where ρ_{l} and ρ_{g} are the densities of liquid and gas, and μ_{l} and μ_{g} are the viscosities of liquid and gas, respectively.

2.3 Validation

As already stated, the principle objective is to see the impingement morphology and the primary breakup spray distribution at a certain transient time. The mesh resolution and the simulation method of the present study need to be verified. There are no universal metrics for judging convergence. For all the numerical simulation results presented, unless otherwise stated, it has been checked that the statistical data are gathered at least three convective times (t_{c}) at the end of the computational domain, where the flow is the most developed and stable, and the downstream situation has no obvious effect on the upstream structure (i.e. spray half cone angle mainly), by ensemble averaging (Herrmann, 2008, 2010). In this study, convective time is defined as the ratio of skip distance to axial sheet velocity ($t_{\mathrm{c}}=L_{\mathrm{s}}/V_{\mathrm{a}}$). At one t_{c}, impingement begins and a spray half cone angle starts to form.

The numerical simulation considers only the primary breakup and ignores the disturbances from the inlets while it is a very complicated situation in experiments. Thus, the spray half cone angle is deemed to be the only valid factor that can be perceived directly. Cheng et al. (2019) obtained experimental results of a liquid-liquid pintle injector element in different LMR situations as shown in Fig. 3a, and flow conditions shown in Table 3. There is no specific velocity magnitude in (Cheng et al., 2019) and it was calculated according to the parameters given by the authors of this paper. The present work

Table 3 Flow conditions of liquids in (Cheng et al., 2019)

Axial liquid (rectangular sheet)					Radial liquid (orifice jet)			
Experimental medium	Length (mm)	Thickness (mm)	Velocity (m/s)	*Re*	Experimental medium	Diameter (mm)	Velocity (m/s)	*Re*
water	15	0.39	9.7	7340	water	1.03	24.5	24500

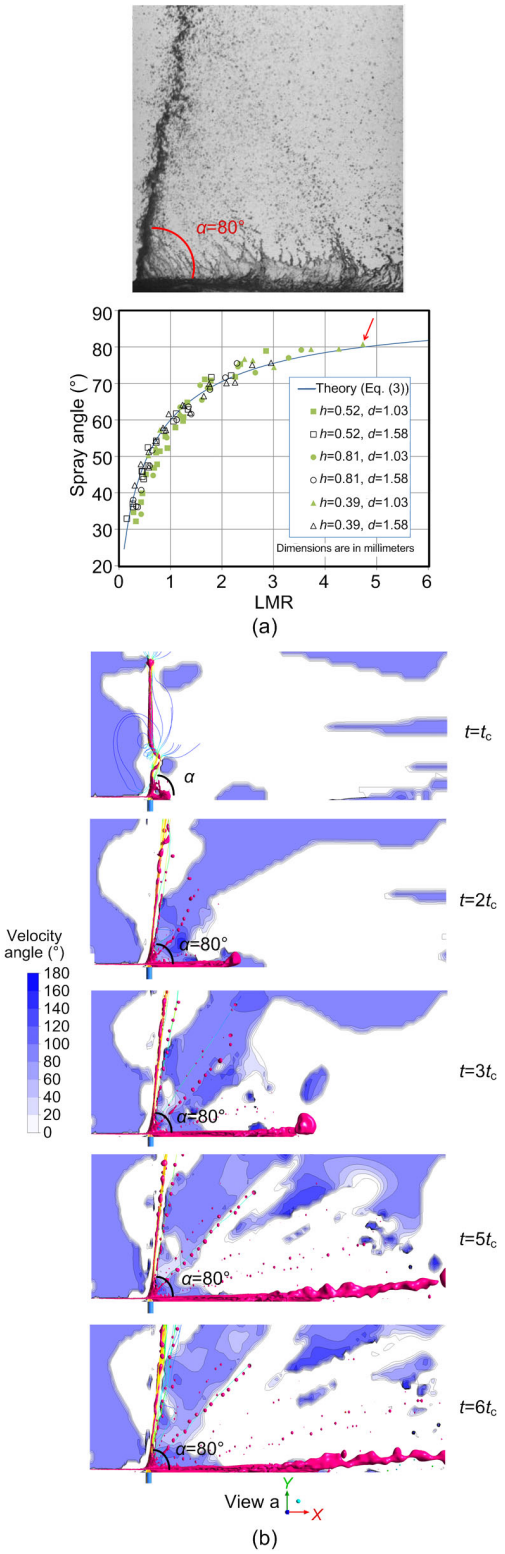

Fig. 3 Simulation verification results: (a) experimental results; (b) simulation results (modified from (Cheng et al., 2019))

h is the film thickness of pintle injector elements and *d* is the jet diameter. References to color refer to the online version of this figure

randomly picked the case (noted in red arrow) to verify the feasibility and the accuracy of the current simulation method as shown in Fig. 3a. The carmine color indicates the iso-surface of liquid volume fraction which is equal to 0.5. From top to bottom, each contour corresponds to each convective time (i.e. t_c, $2t_c$, $3t_c$, $5t_c$, $6t_c$). It shows that after one convective time, the spray half cone angle remains the same although the axial sheet and the radial jet continue developing and the liquid masses can be captured in a physically sound way. So it is reasonable to gather three convective times at $t=3t_c$ to investigate the impingement morphology and the overall primary breakup structure. Computing more than $3t_c$ is not necessary. Furthermore, it can be seen that the numerical simulation spray half cone angle ($\alpha=80°$) is in good agreement with the experimental result at $t=3t_c$.

3 Results and discussion

3.1 Impingement morphology

Fig. 4 shows the impingement morphology at 0.24 ms, 0.28 ms, and 0.32 ms in side view (i.e. view a). The carmine color indicates the iso-surface of liquid volume fraction equal to 0.5. The blue color indicates the wall boundary. Each column corresponds to a time and each row corresponds to a case. At 0.24 ms, the impingement begins. As the radial jet velocity increases, the radial jet gets more momentum to penetrate the axial sheet, and more disturbances are fed into the impinging point. In case B and case B-1, the local momentum of the radial jet is not large enough to totally penetrate the axial sheet, and the

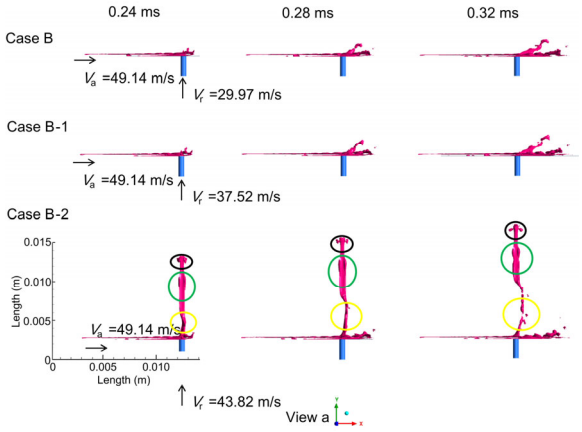

Fig. 4 Impingement morphology in side view

References to color refer to the online version of this figure

formation of a spray half cone angle begins as a result of the resultant velocity. Comparing case B with case B-1, case B-1 shows stronger capillary wave at the impinging point because its radial jet local momentum is larger. In case B-2, the local momentum of the radial jet is too large for the axial sheet to cut-off the radial jet immediately, and the radial jet totally penetrates the axial sheet, forming a mushroom tip (in the black circle) like a jet injecting into quiescent air. Due to surface tension and aerodynamic force under the mushroom tip, wave propagation leads to asymmetric neck destabilization (in the green circle). At 0.28 ms, in case B and case B-1, a clear spray half cone angle forms, and small liquid masses can be captured in front of the axial sheet, where the breakup of the ligaments begins. In case B-2, the edge of the mushroom tip begins to detach, forming liquid masses of a certain size. With continuous effect of surface tension and aerodynamic force on the neck, the neck has a tendency to be pinched-off along the axial direction, and a ligament starts to form along the radial direction (in the yellow circle). A clear spray half cone angle has not been noted. At 0.32 ms, in case B and case B-1, the axial sheet and the impinging spray continue developing along the axial direction with a strong capillary wave. In case B-2, certain size of liquid masses detach from the mushroom tip edge and the ligament along the radial direction as the neck is pinched-off by surface tension. Small satellite liquid masses are captured in the pinch-off region.

Fig. 5 shows the impingement morphology at 0.24 ms, 0.28 ms, and 0.32 ms in front view (i.e. view b). The carmine color indicates the iso-surface of liquid volume fraction equal to 0.5. The blue color indicates the wall boundary. Each column corresponds to a time and each row corresponds to a case. In this perspective, emphasis is mainly put on the impingement morphology at 0.32 ms. In case B and case B-1, a clear hollow structure (in the black circle) forms at the impinging point, and the size of the hollow structure is proportional to the radial jet velocity. In case B-2, the radial jet penetrates the axial sheet strongly, creating intense disturbances on both the radial and axial directions, leading to the formation of cellular ligaments breaking up with small satellite liquid masses around them (in the yellow circle). The hollow structure is not as perfect as in case B and case B-1 due to the larger radial jet momentum.

Fig. 6 shows the impingement morphology at 0.24 ms, 0.28 ms, and 0.32 ms in bird's eye view (i.e. view d). The carmine color indicates the iso-surface of liquid volume fraction equal to 0.5. The blue color indicates the wall boundary. Each column corresponds to a time and each row corresponds to a case. In this perspective, emphasis is mainly put on the impingement morphology of the axial sheet. Case B is an example to illustrate the primary breakup process of one straight ligament (in the black circle). Aerodynamic force and surface tension make this straight ligament a "date pit" shape. The aerodynamic force shapes the pointed tips at both ends, and the tips detach from the ligament core, forming small liquid masses. The surface tension makes the ligament core contract and pinch itself off at the point where the aerodynamic force equals the surface tension, forming a shorter ligament. Case B-1 is an example to

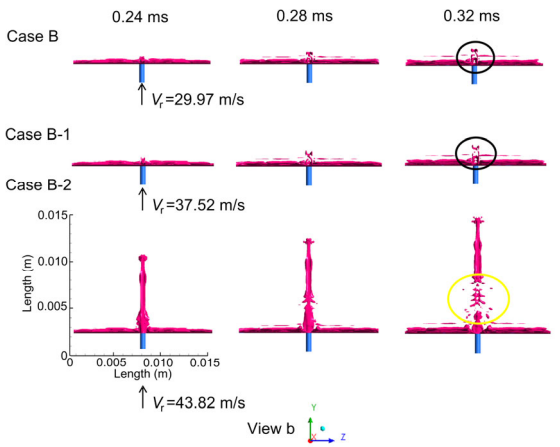

Fig. 5 Impingement morphology in front view
References to color refer to the online version of this figure

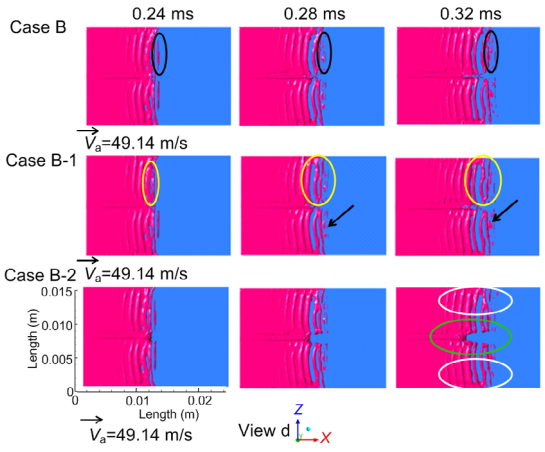

Fig. 6 Impingement morphology in bird's eye view
References to color refer to the online version of this figure

illustrate the formation of a "ring-like" ligament (in the black circle). The hole grows bigger under the aerodynamic force action, making the ligament thinner at a certain point, and finally the "ring-like" ligament gets pinched-off due to surface tension. Meanwhile, due to inertial motion, the re-collision phenomenon is captured, suggesting that the breakup process does not decrease monotonically (black arrow). Furthermore, the re-collision phenomenon can feed disturbances to the axial sheet surface to speed up the development of instability. Case B-2 is an example to illustrate the axial sheet primary breakup pattern. An intermittent disturbed wave occurs on the axial sheet surface, and grows more intense in the front. A small radial jet effect affects the outer rim on the axial sheet, showing a stretched breakup pattern (in the white circle) in the spanwise (i.e. z-direction). Due to the larger radial jet effect, the inner rim shows a cellular breakup pattern (in the green circle), both spanwise and streamwise (i.e. x-direction). Furthermore, the radial jet dominates the primary breakup pattern in the streamwise direction while the axial sheet dominates the primary breakup pattern in spanwise. With radial velocity increasing, the radial jet carries more momentum and the impinging effect becomes stronger and thus more intense disturbances are fed to the surface of the axial sheet.

Fig. 7 shows the formation of vortices during the impingement in front view (i.e. view b). The contour is drawn on a 2D sliced plane at the impinging point, indicating the velocity magnitude. The white line shows the streamline on this sliced plane. Each column corresponds to a time and each row corresponds to a case. At 0.24 ms, the radial momentum and the axial momentum generate aerodynamic force, forming two asymmetric vortices above the axial sheet (red arrow). At 0.28 ms, disturbances on the axial sheet spoil the streamline and the vortices marked by the red arrow disappear. At the same time, two vortices are generated above the impinging point (black arrow) and these vortices develop further at 0.32 ms, feeding more disturbances to the axial sheet surface and the spray liquid. The vortices spotted here are the external energy sources that generate the breakup. Particularly, in case B-2, there are two vortices under the radial jet mushroom tip (yellow arrow) at 0.24 ms, generating breakup from the tip edge as shown in Fig. 4. The vortices develop further as time passes, meaning more instability is developing and thus a continuous breakup can happen. In an ideal 2D situation, the three types of vortices captured here are presumed to be symmetric, whilst in three dimensions, the problem might be stochastic and could lead to an asymmetric situation.

Fig. 8 shows the velocity contour of case B in side view (i.e. view a) at 0.32 ms. The contour is drawn on a 2D sliced plane at the impinging point. The right-hand image is an enlargement of the region marked in black in the left-hand image. Significantly, it shows that the greatest velocity occurs at the impinging point, while under the impinging point (i.e. near the place where the axial wall and the radial wall intersect), there exists a relatively low velocity region,

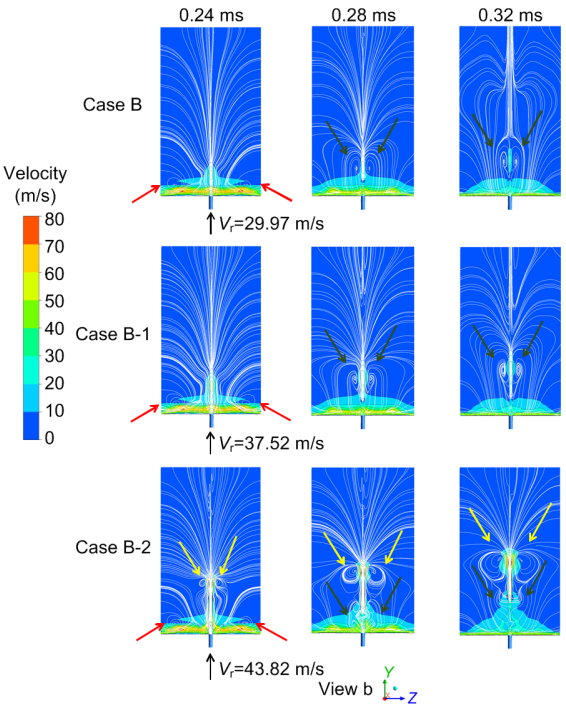

Fig. 7 Formation of vortices
References to color refer to the online version of this figure

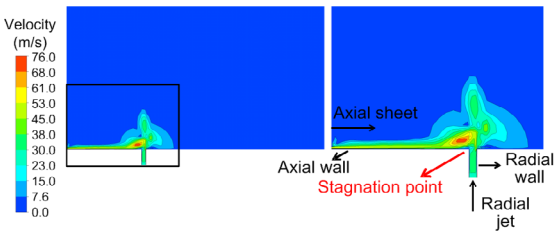

Fig. 8 Illustration of the stagnation point
References to color refer to the online version of this figure

where the velocity is approximately zero. That is the very region that shows a relatively high pressure as shown in Fig. 9. Dombrowski (1963) and Hasson (1964) defined this point as the stagnation point. Fig. 8 is included to demonstrate the existence of the stagnation point with case B as an example. Consideration of the role the stagnation point plays is not an object of the present work.

3.2 Overall primary breakup structure

The overall primary breakup structures are collected at the end of the simulation at $t=3t_c$.

Fig. 9a shows the profile of velocity angle contour, radial jet streamline distribution, particle distribution, and pressure contour in side view (i.e. view a). Fig. 9b is enlargements of the parts in the black boxes marked S in Fig. 9a. The profile is drawn on a 2D sliced plane at the impinging point. Each row corresponds to a case. Particles smaller than 0.5 mm in diameter are mainly captured at the front of the axial sheet and the radial jet, indicating that, due to the local strong aerodynamic force, the primary breakup happens at the front of the axial sheet and the radial jet. Particles marked in the left-hand red rectangles are mainly the result of the primary breakup of the radial jet while particles marked in the right-hand red rectangles are mainly the result of the primary breakup of the axial sheet. With the radial jet velocity increasing, more particles are captured at the fronts of both. This is because a greater radial jet velocity can generate more disturbances to a longer distance and will speed up the breakup. In case B-2, there are no particles smaller than 0.5 mm in diameter captured near the impinging point, while big liquid masses appear. This indicates that simply increasing the radial jet velocity is good for a breakup far from the impinging point rather than promoting one near the impinging point. The radial jet streamline in rainbow colors shows the direction the radial jet travels whilst the velocity angle contour can give a quantitative analysis of the velocity vector which will be verified in future experimental work. Qualitatively, the spray half cone angle is proportional to the radial jet velocity. Fig. 9b shows there is a vortex on the right of the impinging point, as circled in black in case B as well as in case B-1. This vortex is stabilized by the ligament in the resultant velocity direction and the axial sheet. The vortex feeds disturbances to the liquid surface to sustain the breakup process and shape the spray half cone angle clearly. In case B-2, there is no vortex spotted because the intermittent liquid masses in the resultant velocity direction cannot create a stable vortex in a discontinuous velocity vector, as shown in the gap of velocity angle circled in black. In the three cases, the high pressure core circled in black always exists, identifying the location of stagnation point. As the radial jet velocity increases, the pressure core magnitude increases with the high pressure region slightly broadened. It is the result of energy conservation; the

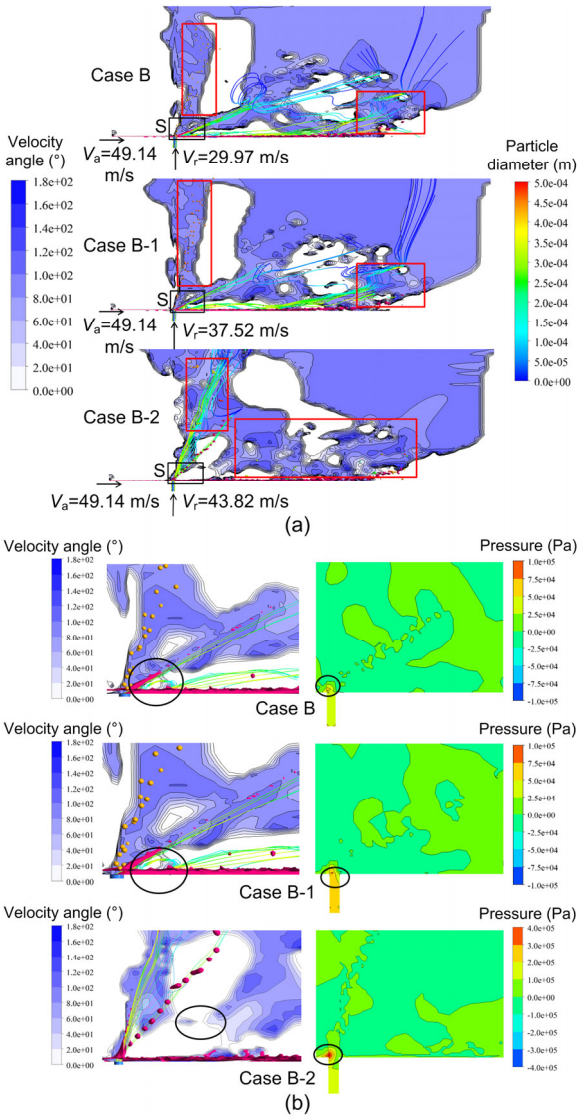

Fig. 9 Profile of velocity angle contour, radial jet streamline distribution, particle distribution, and pressure contour: (a) view a; (b) enlargement of black box S

References to color refer to the online version of this figure

reduced kinetic energy is converted into pressure potential energy.

Fig. 10 shows the lump diameter contour. Lump is a generic term for the axial sheet, radial jet, and the liquid masses produced. With increasing radial jet velocity, the axial lump diameter range before the impingement becomes larger and wider. This is because a greater radial jet velocity leads to stronger impingement, and can thus feed more disturbances to the upstream axial sheet. Meanwhile, a larger radial jet velocity leads to more disturbances conveyed downstream and generates strong aerodynamic force, making the ligaments at the front of the axial sheet shorter and the liquid masses smaller. Case B-2 is an example demonstrating this lump diameter distribution. As stated in Fig. 6, there is a re-collision phenomenon during the primary breakup process. Thus, the lump diameter does not decrease monotonically. As circled in black, there is a region where the lump diameter increases. Due to the surface tension effect, the inner rim diameter is thicker; it is circled in white. At the front of the axial sheet, the lump diameter distribution is homogeneous on one ligament or on one liquid mass.

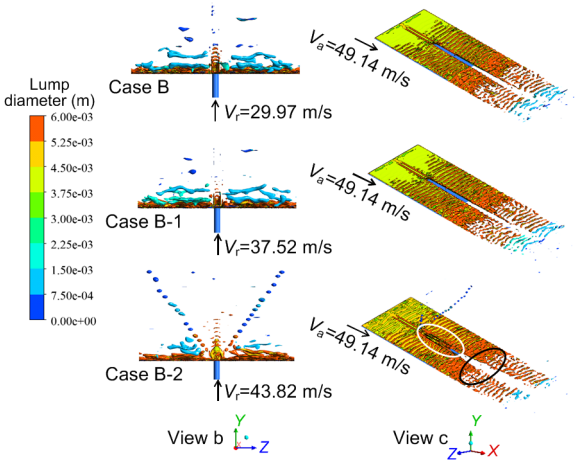

Fig. 10 Lump diameter contour

References to color refer to the online version of this figure

Fig. 11 shows the lump velocity contour. With increasing radial jet velocity, the axial lump velocity magnitude decreases slightly. This is the result of the following three effects. Firstly, a larger radial jet velocity means a larger drag force to the axial sheet to cut-off, and this drag force propagates both spanwise and streamwise, leading to the decrease of the axial lump velocity. Secondly, a larger radial jet velocity leads to stronger impingement, and feeds more disturbances to the upstream axial sheet, and thus lowers the downstream velocity. Thirdly, the re-collision phenomenon during the primary breakup process can weaken the downstream velocity. Case B-2 is an example demonstrating the lump velocity distribution. Due to the surface tension effect, the inner rim velocity magnitude is smaller; it is circled in white. At the front of the axial sheet, the aerodynamic force near the liquid surface deforms the ligaments, and the lump velocity distribution is inhomogeneous on one ligament or on one liquid mass as circled in black. This uneven velocity distribution on one ligament or on one liquid mass explains the occurrence of breakup under the effect of shear force caused by a velocity difference.

Due to larger LMR, case B-2 does not form a perfect hollow structure at the impinging point like the other two cases, which leads to the morphology difference among the three cases. Thus, only in case B-2, there are two separated radial jets in the radial direction. As shown in Fig. 12, the lump circled in the middle figure evolves from the lump indicated by arrows in the left-hand figure. As the impingement continues, the whole system achieves dynamic stability and the lumps in the black circles develop in the directions marked black in the right-hand figure. Figs. 10 and 11 share the same lump morphology except that the contour colors represent lump diameter and lump velocity, respectively.

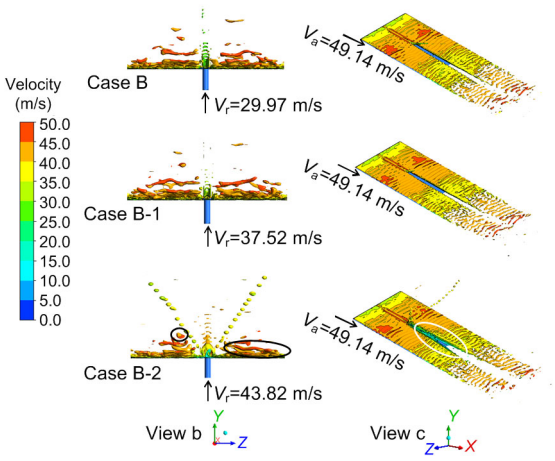

Fig. 11 Lump velocity contour

References to color refer to the online version of this figure

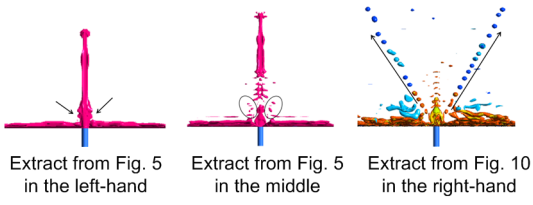

Fig. 12 Additional explanation of case B-2
References to color refer to the online version of this figure

4 Conclusions

The present study has focused on the impingement morphology, the formation of primary breakup spray half cone angle, the pressure distribution, the liquid diameter distribution, and the liquid velocity distribution in a liquid on liquid pintle injector element with different radial orifice jet velocities.

The mushroom tip of the radial jet is captured after the penetration to the axial sheet, and disturbances generated behind the tip form vortices that aid the breakup of the tip edge. The hollow structure near the impinging point is spoiled when the radial TMR is too large, and breakup into cellular ligaments happens more obviously instead. The straight ligament breakup and the "ring-like" ligament breakup of the axial sheet are discussed. Aerodynamic force and surface tension both play an important role. The impingement process can generate new vortices near the impinging point to sustain the energy source of the breakup.

The spray half cone angle is proportional to the radial jet velocity. The primary breakup mainly happens at the front of the axial sheet or the radial jet and at the impinging point. A larger radial jet velocity can feed more disturbances on the axial sheet for a longer distance. A high pressure core is spotted, demonstrating the existence of a stagnation point in a liquid-liquid impinging situation. Due to the surface tension effect, the velocity magnitude of the inner rim on the axial sheet is smaller and the lump diameter magnitude is larger. The velocity of the inner rim on the axial sheet becomes smaller as the radial jet velocity increases and, because of re-collision phenomenon, the lump diameter magnitude of the axial sheet does not decrease monotonically during the breakup process.

Contributors

Rui ZHOU wrote the first draft of the manuscript and edited the final version. Chi-bing SHEN guided the work of the paper. Xuan JIN provided the additional help.

Conflict of interest

Rui ZHOU, Chi-bing SHEN, and Xuan JIN declare that they have no conflict of interest.

References

Cheng P, Li QL, Xu S, 2017. On the prediction of spray angle of liquid-liquid pintle injectors. *Acta Astronautica*, 138: 145-151. https://doi.org/10.1016/j.actaastro.2017.05.037

Cheng P, Li QL, Chen HY, 2019. Flow characteristics of a pintle injector element. *Acta Astronautica*, 154:61-66. https://doi.org/10.1016/j.actaastro.2018.10.020

Dombrowski N, 1963. The aerodynamic instability and disintegration of viscous liquid sheets. *Chemical Engineering Science*, 18:203-214. https://doi.org/10.1016/0009-2509(63)85005-8

Dressler GA, 2000. TRW pintle engine heritage and performance characteristics. 36th AIAA/ASME/SAE/ASEE Joint Propulsion Conference and Exhibit, Article 2000-3871. https://doi.org/10.2514/6.2000-3871

Dressler GA, 2006. Summary of deep throttling rocket engines with emphasis on Apollo LMDE. 42nd AIAA/ASME/SAE/ASEE Joint Propulsion Conference and Exhibit, Article 2006-5220. https://doi.org/10.2514/6.2006-5220

Elverum PS, Miller J, 1967. The descent engine for the lunar module. 3rd Propulsion Joint Specialist Conference, Article 1967-521. https://doi.org/10.2514/6.1967-521

Fang XX, Shen CB, 2017. Study on atomization and combustion characteristics of LOX/methane pintle injectors. *Acta Astronautica*, 136:369-379. https://doi.org/10.1016/j.actaastro.2017.03.025

Giuliano TL, Adamski WM, 2007. CECE: a deep throttling demonstrator cryogenic engine for NASA's lunar land. 43rd AIAA/ASME/SAE/ASEE Joint Propulsion Conference and Exhibit, 2007-5480. https://doi.org/10.2514/6.2007-5480

Hasson D, 1964. Thickness distribution in a sheet formed by impinging jets. *International Engineering Journal*, 10(5): 752-754. https://doi.org/10.1002/aic.690100533

Herrmann M, 2008. A balanced force refined level set grid method for two-phase flows on unstructured flow solver grids. *Journal of Computational Physics*, 227(4):2674-2706. https://doi.org/10.1016/j.jcp.2007.11.002

Herrmann M, 2010. Detailed numerical simulations of the primary atomization of a turbulent liquid jet in crossflow. *Journal of Engineering for Gas Turbines and Power Transactions of the ASME*, 132(6):1-10. https://doi.org/10.1115/1.4000148

James B, Jacob H, 2019. Spray cone formation from pintle-type injector systems in liquid rocket engine. AIAA SciTech 2019 Forum, 2019-0152. https://doi.org/10.2514/6.2019-0152

Kanmaniraja R, Keonwoong L, 2018. Effect of injection conditions on mixing performance of pintle injector for liquid rocket engines. *Acta Astronautica*, 150:105-116. https://doi.org/10.1016/j.actaastro.2017.12.012

Kazuki S, Shinji N, 2015. Optical measurements of ethanol/liquid oxygen rocket engine combustor with planar pintle injector. 51st AIAA/SAE/ASEE Joint Propulsion Conference, 2015-3845. https://doi.org/10.2514/6.2015-3845

Kazuki S, Shinji N, 2017. Combustion characteristics of ethanol/liquid-oxygen rocket-engine combustor with planar pintle injector. *Journal of Propulsion and Power*, 33(2):514-521. https://doi.org/10.2514/1.B36144

Nardi RV, Pimenta A, 2015. Experiments with pintle injector design and development. 51st AIAA/SAE/ASEE Joint Propulsion Conference, 2015-3810. https://doi.org/10.2514/6.2015-3810

Ninish S, Nandakumar K, 2018. Spray characteristics of liquid-liquid pintle injector. *Experimental Thermal and Fluid Science*, 97:324-340. https://doi.org/10.1016/j.expthermflusci.2018.03.033

Son M, Jaye K, 2015. Effects of momentum ratio and Weber number on spray half angles of liquid controlled pintle injector. *Journal of Thermal Science*, 24(1):37-43. https://doi.org/10.1007/s11630-015-0753-7

中文概要

题　目： 针栓式喷注器单元液/液撞击的一次破碎形态的仿真研究

目　的： 针对液/液针栓式喷注器单元，研究其在不同径向射流喷注速度下的一次破碎形态，并阐明在一次破碎下喷雾半锥角的形成、压力场分布、喷雾粒径分布与速度场分布。

创新点： 通过流体体积函数转换离散相（VOF-to-DPM）模型，结合网格自适应（AMR）技术还原了针栓式喷注器单元液/液撞击的一次破碎形态。

方　法： 1. 通过 VOF-to-DPM 模型完成一次破碎过程中对液相的捕捉；2. 采用计算流体动力学后处理（CFD-post）模块进行后处理，得到一次破碎下喷雾半锥角的形成以及压力场、喷雾粒径与速度场的分布云图；3. 在仿真计算过程中使用 AMR 技术减少计算量，节约时间成本与计算资源。

结　论： 1. 速度大的径向射流在穿透轴向液膜后会形成一个蘑菇状的头部；扰动在蘑菇状顶端下方形成涡，有助于蘑菇状顶端边缘破碎的发生。2. 气动力和表面张力对轴向液膜破碎过程中产生的直液丝和环状液丝的破碎起到重要作用；由于液滴的聚合现象，轴向液膜的直径在破碎过程中并不是单调递减的。3. 喷雾半锥角的大小和径向射流速度的大小成正比；一次破碎首先发生在轴向液膜前沿、径向射流头部以及撞击点附近。4. 在表面张力的作用下，轴向液膜内边缘的速度较小，直径较大；当径向射流的速度增大时，轴向液膜内边缘的速度值减小得更加明显。

关键词： 针栓式喷注器单元；液/液撞击；一次破碎；VOF-to-DPM 模型；AMR 技术